New experimental developments for in situ XAFS studies of chemical reactions under hydrothermal conditions

Markus M. Hoffmann, John G. Darab, Steve M. Heald [1], Clement R. Yonker, John L. Fulton [*]

Environmental and Health Sciences Division, Pacific Northwest National Laboratory, Richland, WA 99352, USA

Abstract

New experimental developments for in situ X-ray absorption fine structure spectroscopy (XAFS) studies of hydrothermal systems are described. Improvements in materials of construction and the design of spectroscopic cells have allowed application of XAFS as a powerful method to derive the molecular structures of reacting species. Two different spectroscopic cells are described that are suitable for in situ XAFS studies of aqueous solutions under hydrothermal conditions. One cell consists of a titanium alloy body with a corrosion-resistant platinum–iridium insert and diamond windows for X-ray transmission. Using this cell, XAFS spectra were acquired on aqueous tungstate solutions up to 400°C. The results demonstrate how XAFS can be used to study the speciation of isopolytungstates and their equilibria at high temperatures. Results from model calculations using the FEFF ab initio code are used to explain the observed spectral changes with changes in pH and temperature. The second XAFS cell consists of a simple fused-silica capillary having a 180 μm inner diameter. High-quality spectra of a 0.2 molal nickel bromide solution were collected in these small capillaries demonstrating the feasibility of the approach to the study of a wide range of geochemical systems. Further, the XAFS spectra show that the nickel bromide solution irreversibly reacts with the fused-silica capillary at 425°C. Based upon these observations, a potential use of the fused-silica capillary is suggested for in situ studies of silicate formation, or, in general, for studies of chemical interactions of hydrothermal brine solutions with quartz. © 2000 Elsevier Science B.V. All rights reserved.

Keywords: X-ray absorption fine structure spectroscopy (XAFS); Hydrothermal solutions; Sodium tungstate; Nickel bromide; Quartz

1. Introduction

X-ray absorption fine structure spectroscopy (XAFS) is a well recognized and widely used experimental tool in the geochemical community. XAFS provides short-range structural information such as interatomic distances and coordination numbers, whereas additional valuable information on oxidation state and coordination symmetry can be obtained from the near-edge structure (XANES). Comprehensive reviews on this subject have appeared (Teo, 1986; Brown et al., 1988; Koningsberger and Prins, 1988). Despite the wide use of XAFS for the analysis of solid samples and liquid samples at ambient conditions, the number of XAFS studies applied on

---

[*] Corresponding author. Fax: +1-509-376-0418.

E-mail address: jl_fulton@pnl.gov (J.L. Fulton).

[1] Assigned to PNC, Advanced Photon Source, Argonne National Laboratory.

chemical systems at hydrothermal conditions, i.e., at high temperatures and pressures, is very limited. The focus of these studies has been on the hydration and complexation of ions in aqueous solutions, including the hydration of Sr^{2+} to 385°C (Pfund et al., 1994), Sr^{2+} and Cd^{2+} to 300°C (Seward et al., 1995), Ag^{+} to 350°C, (Seward et al., 1996), Rb^{+} to 425°C (Fulton et al., 1996a,b), Br^{-} to 475°C (Wallen et al., 1997) and Ni^{2+} to 425°C (Wallen et al., 1998), and the complexation of cobalt(II) and cadmium(II) chloride to 200°C (Mosselmans et al., 1996), antimony(III) chloride to 250°C (Oelkers et al., 1998), and copper chloride solutions to 175°C (Collings et al., 1998). Contact ion-pair formation at hydrothermal conditions has been observed and characterized in detail for aqueous nickel bromide solutions at 425°C incorporating molecular dynamics simulation in the analysis of the data (Wallen et al., 1998). The speciation of aqueous yttrium solutions has also recently been studied to 340°C by Ragnarsdóttir et al. (1998).

Undoubtedly the limited number of XAFS studies at hydrothermal conditions reflects the technical difficulties associated with hydrothermal experiments, namely the handling of chemically aggressive samples at high temperatures and pressures. We also recognize that XAFS can be applied beyond the scope of studying the solvation of ions to the broad area of inorganic hydrothermal chemistry. Chemical reactions may alter atomic distances, coordination numbers and symmetry, and oxidation states. In principle, all of these chemical changes can be detected in situ using XAFS. Hence, our most recent efforts have been to further develop the application of XAFS on in situ studies of hydrothermal systems in two directions: (a) to conduct XAFS studies of hydrothermal systems which undergo chemical reactions, and (b) to develop new, chemically resistant spectroscopic cells.

In this article we demonstrate how XAFS can probe structural changes in the hydrolysis equilibria of aqueous tungstate solutions. These equilibria involve isopolytungstates of rather complex (Keggin) structures. Using the FEFF ab initio code (Zabinsky et al., 1995), we qualitatively demonstrate how the structural changes associated with the equilibria affect the observed XAFS data. Wesolowski et al. (1984) pointed out in their carefully conducted

potentiometric study of tungsten VI hydrolysis equilibria to 300°C, that knowledge of the speciation and equilibria at high temperatures is required for an understanding of ore formation processes and extraction processes of the strategic metal tungsten from ores. Besides this study, we are only aware of two Raman studies that carried out in situ measurements of aqueous tungstate solutions to temperatures exceeding 100°C, namely the studies by Bilal et al. (1986) to 200°C, and by Kiddie and Wood (1993) to 300°C. We present XAFS data on this system covering temperatures up to 400°C and pressures up to 450 bar.

Detailed descriptions of cell designs suitable for hydrothermal experiments can be found in Fulton et al. (1996a,b), Mosselmans et al. (1996) and Suleimenov and Seward (1999). Other XAFS cell descriptions suitable for non-aqueous high temperature fluids have appeared too (Murata et al., 1995; Tamua et al., 1995). Diamond anvil cells have also been used for hydrothermal X-ray experiments at high temperatures and pressures (Huang et al., 1994; Bassett and Wu, 1998). The improved design presented here reduces the number of materials in direct contact with the aqueous solution at hydrothermal conditions to two: a platinum–iridium alloy and diamond as the X-ray window material. Both belong to a small class of materials that can withstand the extreme corrosivity of water at low and high pH values and are suitable for studying many reacting chemical systems. There are many features of the overall cell design that are particularly attractive for studies of hydrothermal chemistry. First of all, the pathlength can be chosen between about 1 mm to 10 cm. This is important since many of the systems of interest are at moderate to very low concentrations (0.5 M–1 mM). Furthermore, the cell can be used in fluorescence mode using a backscattering geometry to explore very dilute systems of low-Z atoms (Wallen et al., 1997). Finally, the pressure can be measured directly to within ±1 bar with an electronic pressure transducer. It is especially important to know the pressure precisely since the systems of interest are highly compressible. The ease of sample preparation means that a wide range of PVT conditions and concentrations can be explored in a relative short time thus capturing a better global picture of the hydrothermal chemistry.

An alternative, less expensive approach to conducting XAFS on hydrothermal systems involves the use of fused-silica capillaries. As Wallen et al. (1996) reported, inexpensive high-pressure fused-silica capillaries may be used as XAFS cells. NMR experiments of aqueous resorcinol solutions were subsequently carried out to high temperatures by Bai et al. (submitted) using the fused-silica capillaries. We will show that these capillaries function not only well under extreme hydrothermal conditions but also that with the availability of third-generation synchrotron X-ray sources, with immensely improved beam brightness and flux, high-quality XAFS spectra can be obtained. One limitation of the fused-silica capillaries is that silica dissolves appreciably in water at high temperatures. However, one can take advantage of this fact. We report here a rapid chemical reaction at 425°C of a 0.2 molal nickel bromide solution with the fused-silica capillary to form a nickel silicate. This observation demonstrates the feasibility of using the fused-silica capillaries for in situ studies of silicate formation in hydrothermal solutions or to study interactions of silicates with hydrothermal brine solutions in general. We note that the capillary cell may be also of interest for those who study fluid inclusions in quartz that contains carbon dioxide mixtures at very high pressures.

In addition to the geochemical considerations another motivation for our studies of aqueous solutions at high temperatures concerns the remediation of mixed chemical and radioactive waste streams. Worldwide there are enormous quantities of highly radioactive waste streams that await stabilization through vitrification and other means into a waste form for final storage. Proposed vitrification of these complicated waste mixtures will involve processes operating at temperatures up to or exceeding 1200°C (Darab and Smith, 1996). Spectroscopic studies of these aqueous waste streams (both actual and simulated) under ambient conditions, of the intermediate dried and calcined waste, of the melts, and of the final glass have previously been performed. However, the initial stages of these processes, which occur at temperatures above 100°C but before the water has been driven off (i.e., hydrothermal conditions), involve complicated redox, inorganic polymerization, and complexation chemistry, but have not yet been studied. The chemistry that occurs during these initial processing stages are important in determining the chemistry at much higher temperatures in the melt stage (Darab and Smith, 1996), but is often overlooked. Hence, a basic understanding of fundamental chemistry at elevated temperatures is urgently needed to guide these waste treatment processes.

2. Experimental

2.1. Pt / Ir XAFS cell design

Fig. 1 shows a schematic drawing of the Pt/Ir XAFS cell. The design has a working pressure of 1.5 kbar at 600°C. A small Pt/Ir (90/10) insert (2 mm I.D., 16 mm O.D., 2.5 mm long) was press-fit into the main body (mm O.D.) made from Ti6Al4V alloy (Ti-6-4). Final machining was done after stress-relieving the assembly by heat treatment to 650°C. The body of the cell accepts four, 3.2-mm diameter × 5 cm long resistive heaters (50 W each). Two additional 3.2-mm holes accommodate platinum resistance probes for temperature measurements. The cell was attached to a light-frame stand made from machinable ceramic (RESCOR, Cotronics) and was held in place by a ceramic screw.

The diamond windows are sealed directly onto the Pt/Ir insert using a ''squeezer'' type of design (Sherman and Stadtmuller, 1987). The diamond window is pressed against a polished Pt/Ir surface using a series of high-temperature disc springs (Schnorr) loaded against the retaining nut. Synthetic, single crystal type 1B diamonds having a 1,1,0 orientation were used during acquisition of the tungstate data.
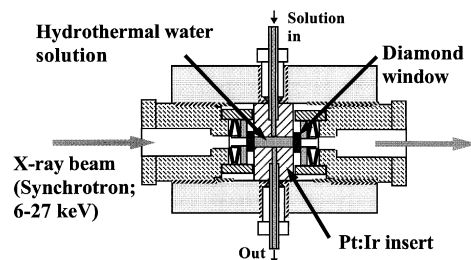

Fig. 1. Schematic drawing of the high pressure/high temperature XAFS cell with Pt/Ir insert and diamond windows. The design is rated for 1.5 kbar at 600°C.

The diamond windows were 1 mm thick and 3 mm in diameter.

It is essential to the acquisition of low-noise XAFS spectra to obtain high-temperature uniformity within the cell to minimize convective fluctuations of the fluid. Several layers of insulating glass fiber blanket interleaved with aluminum foil were molded around the cell to act as a thermal radiation barrier. In order to eliminate further heat losses through convection, the whole cell was placed in an aluminum vacuum can. Although instances of failure are rare, the aluminum vacuum enclosure also served as a protective shield. The X-ray beam entered the vacuum enclosure through small holes covered by a thin polyimide (Kapton) tape.

2.2. Capillary set-up

Wallen et al. (1996) were able to obtain a XAFS spectrum of an organometallic compound in supercritical carbon dioxide confined in a fused silica capillary of 250 μm I.D. and 360 μm O.D. Here we describe a very simple set-up that utilizes fused silica capillaries for XAFS experiments under hydrothermal conditions.

The schematic in Fig. 2 shows how the capillary was aligned relative to the X-ray beam and the fluorescence detector. A piece of fused-silica capillary tubing (Polymicro Technologies) of 180 μm I.D. and 340 μm O.D. and about 30 cm in length was inserted into a four hole ceramic tube (Omega, Omegatite 200) that served as a holder. A small portion (8 mm long) of this ceramic tube was ground away such that the capillary in this region is completely exposed to the X-ray beam and that the fluorescence emission has free passage to the fluo-
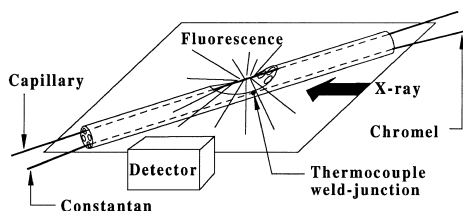

Fig. 2. Details of the capillary alignment relative to the X-ray beam and fluorescence detector. A chromel–constantan thermocouple junction measures the temperature.

rescence detector. A bare chromel–constantan (Type E) thermocouple wire was also inserted in the ceramic tube in the hole adjacent to the capillary as close as possible to the XAFS region. The capillary was aligned 45° with respect to the X-ray beam and the fluorescence emission was detected at 90°, again with respect to the X-ray beam.

The ceramic tube containing the capillary and thermocouple was ''sandwiched'' between two halves of a cylindrical ceramic fiber heater (Watlow). This commercially available heater (5 cm I.D., 15 cm O.D., 20 cm long) was slightly modified to provide ports for the X-ray beam, the capillary and the fluorescence emission.

The capillary was connected to standard high-pressure 1.6-mm tube fittings (High Pressure Equipment) using a Vespel® ferrule and a small brass back-up ring in place of the standard ferrule in a cool region outside of the heater. The capillary was stress-relieved by securing these capillary connectors firmly in place. A simple holder for the heater assembly was mounted on a tilt stage that allowed the capillary to be aligned to the 2 mm wide by 100 μm high x-ray beam.

2.3. Sample preparation

The chemicals $Na_2WO_4.2H_2O$ (Alfa Aesar, 99%), $NiBr_2$ (Alfa Aesar, 99%) and HPLC grade water (Aldrich) were used as received for all solutions prepared. The pH of the tungstate solutions was adjusted with concentrated nitric acid (Aldrich 99.999%). All reported pH values are starting pH values, i.e., the pH values were measured before the sample was introduced into the XAFS cell and brought to experimental conditions of temperature and pressure. In order to minimize dissolved oxygen in the solutions, high-purity nitrogen gas was vigorously bubbled through the 50-ml solutions for 15 min. prior to transfer into the XAFS cell.

A simple, efficient method to introduce samples into the high temperature cell was implemented. The method involves the use of Teflon sample bags that are placed inside a high-pressure vessel (Busey et al., 1984) that is connected to a standard syringe pump (ISCO Model 100DX). The contents of these bags can then be transferred to the hydrothermal XAFS

cell in about 15 min through 1.6-mm diameter transfer lines that are constructed from corrosion-resistant materials (e.g., platinum or titanium alloys). Thus, the widest range of chemical systems can be studied.

The pressure of the system was monitored within ± 1 bar with a calibrated electronic transducer (Precise Sensors. No. D451). The temperature of the XAFS cells was controlled to an accuracy of $\pm 3°C$ using a three-mode controller (Omega, No. CN3000). As a general safety measure, an additional redundant temperature limit controller (Watlow, Series 94) was placed in series with the three-mode temperature controller.

2.4. Data acquisition

Most of the data presented here were obtained on the PNC-CAT beam line (ID-20) at the Advanced Photon Source (APS) at Argonne National Laboratory. Both the undulator and monochromator (Si 111 crystal) were scanned for XAFS spectra acquisition. The monochromator was detuned 30% for rejection of higher harmonics. The energy stability of the monochromator was monitored with appropriate standards during all measurements. The tungstate spectra were acquired in transmission mode using the Pt/Ir cell described below. For the fused-silica capillaries, spectra were acquired in fluorescence mode using a standard ion chamber filled with nitrogen gas. The unfocused beam passed through a 1.5-mm diameter pinhole or a 100-micron wide $\times 2$ mm long slit before the I_o chamber in front of the Pt/IR and capillary cell, respectively. In each case, the remaining beam passed cleanly through the sample. The position of the pinhole/slit and the sample cell were adjusted to optimum positions relative to the beam using X–Y stepper motors.

A few of the tungstate spectra (pH ≤ 5.5) were acquired at beam line X-19A (bending magnet) at the National Synchrotron Light Source of Brookhaven National Laboratory. Here, the beam was focused to 2 mm in diameter after the Si (111) crystal monochromator. These data were also taken in transmission mode.

2.5. Data treatment and analysis

We used an automated background subtraction method (AUTOBK) developed by Newville et al.

(1993) for this procedure to subtract $\chi(k)$ from the tungstate data. The minimum R-space distance, R_{bkg}, required as input variable in AUTOBK, was chosen for all data as 1.0. The strongly absorbing ''white line'' was kept in the fitted k-range for background subtraction to assure consistent subtraction of background for all tungstate data including the data at low pH. The E_o value was defined in this work by the maximum in the first derivative in the edge region. All radial structure plots presented are from Fourier transformations of k^3-weighted $\chi(k)$ functions in the k-range 3 Å $< k < 12$ Å, employing Hanning-windows. Prior to this background removal treatment some diffraction-related background peaks from the 1 B diamonds that were used to acquire the tungstate spectra in the Pt/Ir cell were removed simply by deleting one or two affected data points because these diffraction peaks were sharp and well defined.

For further analysis of the $\chi(k)$ functions of the tungstate data at pH 8.5 the standard XAFS relationship

$$\chi(k) = \frac{F(k)S_0^2 N}{kR^2} e^{-2k^2\sigma^2} e^{-2R/\lambda(k)}$$

$$\times \sin\left(2kR + \delta(k) - \frac{4}{3}k^3 C_3\right) \qquad (1)$$

was used. $F(k)$, $\delta(k)$ and $\lambda(k)$ are the amplitude, phase, and mean-free path factors, respectively, that are derived from a calculation on a theoretical standard using the FEFF-code (Zabinsky et al., 1995). The crystallographic data on Na_2WO_4 by Okada et al. (1974) served as a basis for the atomic configurations used for the FEFF calculations. The Debye–Waller factor σ^2 represents the mean-square variation of the shell distance R due to both the static and thermal disorder while C_3 is the anharmonicity of the pair-distribution. Finally, S_0^2 is a constant value, representing the core-hole factor. The coordination number N was set to 4 for the tetrahedrally coordinated WO_4^{2-}. In addition to the structural parameters, a single non-structural parameter, ΔE_o, is varied to account for the simple estimate of this energy made by FEFF. A refined ΔE_o value of 7 eV above the first W_{L-III} edge inflection point was used. In order to obtain the structural parameters σ^2, R, and C_3, and the core-hole factor S_0^2, the room-temperature

0.2 m Na_2WO_4 spectrum was first fitted using the FEFFIT program (Newville et al., 1995; Stern et al., 1995) that employs a nonlinear, least-squares fit to the theoretical standard calculated by FEFF (Zabinsky et al., 1995). The obtained value for $S_0^2 = 0.95 \pm 0.05$ was then used for fitting the remaining spectra at higher temperatures. We fitted the data in the k-range 3 $\text{Å}^{-1} < k < 14$ Å^{-1}. The statistical noise for the (small) C_3 values was too large to precisely determine this parameter. Hence, this parameter was fixed to an average value of $C_3 = -6 \times 10^{-5}$ Å^{-3} for a final fitting. The uncertainties for the obtained Debye–Waller factors and W–O bond distances are ± 0.0003 Å^2 and 0.007 Å, respectively.

3. Results and discussion

3.1. Results on 0.2 molal aqueous sodium tungstate, pH 8.5

Dissolving a sodium tungstate salt in water leads to an aqueous solution of tetrahedrally coordinated WO_4^{2-} solvated anions (Kepert, 1973) at a pH of 8.5. In Fig. 3 we show the ($W_{\text{L-III}}$) absorption spectrum $\mu(E)$ of such a Na_2WO_4 solution (0.2 molal) at 200°C and 207 bar, and 400°C and 450 bar. Both spectra were acquired in a single 20-min scan. Both spectra display a damped sinusoidal oscillation in the XAFS region originating from the four tetrahedral oxygens. Because the edge height is proportional to the number of absorbing atoms and because the path
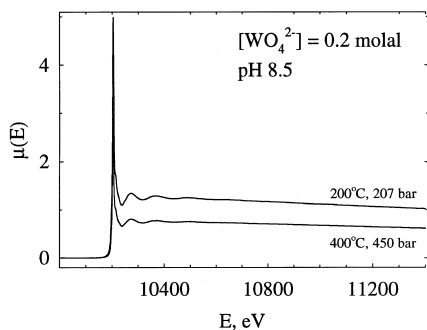

Fig. 3. Absorption spectrum at the $W_{\text{L-III}}$ edge of a 0.2 molal Na_2WO_4 aqueous solution at 200°C, 207 bar and 400°C, 450 bar. The smaller edge height at 400°C corresponds to a lower density at this temperature as explained in the text.

length of the cell and the molal (and mole ratio) concentration of the solutions are fixed, the height of the edge provides a convenient and important measurement of the density (Fulton et al., 1996a,b). The height of the absorption edge is substantially smaller at 400°C compared to 200°C owing to the lower density at these temperature and pressure conditions.

Fig. 4 not only shows the k^3-weighted XAFS oscillation and corresponding radial structure plots of the two traces from Fig. 3 but also include the data for 25°C and 200°C at 235 bar (NSLS data set), and the 25°C data (APS data set). The main peak in the Fourier transforms of the NLSL data are slightly larger compared to the APS data at same temperatures. However, within each data set very little or no change is apparent with increasing temperature. As a first result, we therefore conclude that the WO_4^{2-} anion in the 0.2 m solution stays intact upon heating to 400°C, i.e., that the tungsten atom remains surrounded by four oxygen atoms in tetrahedral coordination. Table 1 shows the results of the detailed XAFS analysis, as described in the previous section, of the 0.2 molal Na_2WO_4 solution spectra at pH 8.5. Within experimental scatter, the tungsten−oxygen bond distance of 1.782 ± 0.007 Å in the WO_4^{2-} anion does not change with temperature. The Debye–Waller factor increases with temperature from 0.0015 Å^2 at 25°C to 0.0021 Å^2 at 250°C and 0.0022 Å^2 at 400°C. Compared to room temperature, Wood observed at 270°C in his Raman measurements a 4 cm^{-1} shift to lower wavenumbers for the total symmetric stretching mode, nominally at 930 cm^{-1} (personal communication). Within a diatomic approximation, the vibrational contribution to the Debye–Waller factor, σ_{vib}, is related to the vibrational frequency (cm^{-1}), the force constant K (mdynes/Å) and temperature (K) by (Cyvin, 1968)

$$\sigma_{\text{vib}} \sim \left[(\tilde{v}/K)\coth(y/2) \right]^{1/2} \qquad (2)$$

$$\sigma_{\text{vib},1}/\sigma_{\text{vib},2} = \left[(\tilde{v}_1/\tilde{v}_2)(K_2/K_1) \right.$$
$$\left. \times (\coth(y_1/2)/\coth(y_2/2)) \right]^{1/2} \qquad (2a)$$

with $y = 1.441(\tilde{v}/T)$. Based on this equation, the observed 4 cm^{-1} change in frequency amounts to a negligibly small change in the Debye–Waller factor.
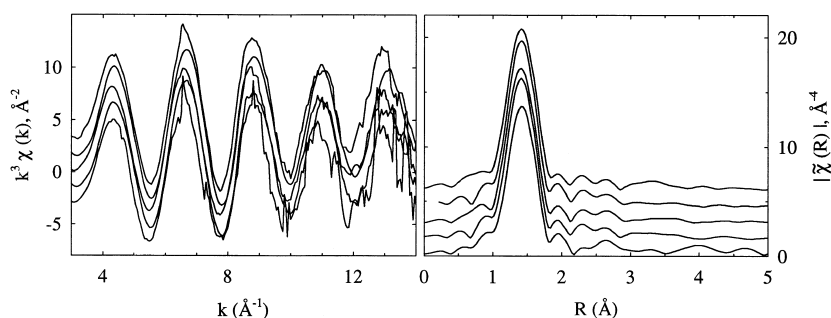
Fig. 4. The $\chi(k)$ function and corresponding radial structure plot of five 0.2 molal Na_2WO_4 solutions at pH 8.5; from top to bottom: 25°C, 1 bar, APS data; 25°C, 1 bar, NSLS data; 200°C, 207 bar, APS data; 200°C, 235 bar, NSLS data; 400°C, 450 bar, APS data. For clarity, the graphs are offset by a constant value relative to the 400°C data. Within experimental error there is no change in the W–O bond distance with increasing temperature.

The temperature increase from 25°C to 270°C would only account for an increase of the Debye–Waller factor by less than 10%. Hence, the observed 30% to 40% increase of the Debye–Waller factor to high temperatures indicates a slight reduction in the W–O bond strength and/or increase of the structural disorder. It should be noted that possible contributions from second shell water molecules to the fine structure oscillations would be negligibly small because of their large structural disorder and large bond distances.

Densities of the 0.2 molal aqueous Na_2WO_4 solutions are also listed in Table 1. The density value at room temperature was obtained with a density meter employing a vibrating tube. All other values were obtained from the absorption edge height as explained in this section.

Table 1
XAFS analysis of 0.2 m aqueous Na_2WO_4 solutions to 400°C, pH 8.5.

T (°)	P (bar)	ρ (g/cm^3)	R_{W-O} (Å)	σ^2 (Å^2)	$\Re$[a]
25	1	1.05	1.780	0.0015	0.014
100	235	1.02	1.777	0.0017	0.021
150	235	0.98	1.778	0.0018	0.019
200	207	0.92	1.789	0.0020	0.021
200	235	0.93	1.783	0.0018	0.016
250	180	0.87	1.789	0.0021	0.015
400	450	0.57	1.789	0.0022	0.047

[a] Goodness of fit defined by a scaled sum of squares as described in FEFFIT (Newville et al., 1995; Stern et al., 1995).

3.2. Acidification of a 0.2 molal Na_2WO_4 solution at room temperature

3.2.1. Observations

Acidification of solutions of the normal tungstate, WO_4^{2-}, leads to the formation of isopolytungstate anions, containing clusters of corner- and edge-shared octahedrons. A large number of studies have been carried out to characterize and quantify the species involved in these very complex isopolytungstate equilibria. These attempts have been reviewed a number of times including Evans (1971), Kepert (1973), Cotton and Wilkinson (1980), and Greenwood and Earnshaw (1984). Despite these extensive studies, a complete understanding of the isopolytungstate system has not been reached thus far. However, a general, simplified, reaction scheme seems to have reached common agreement (Kepert, 1973; Greenwood and Earnshaw, 1984). In this scheme, initial acidification leads to a paratungstate (A) $[HW_6O_{21}]^{5-}$ at a pH of about 6, to a pseudo-metatungstate $[HW_6O_{20}]^{3-}$ at a pH of about 4 and to a $WO_3 \cdot 2H_2O$ precipitate at a pH of about 1. While the kinetics for these equilibria are fast, the initially formed paratungstate (A) and pseudo-metatungstate are subject to further very slow aging at room temperature to form paratungstate (B or Z) $[H_2W_{12}O_{42}]^{10-}$ and metatungstate $[H_2W_{12}O_{40}]^{6-}$. In light of this reaction scheme and the different kinetics involved, it is important to mention that the spectra reported in this section were obtained within a few hours after the samples had been prepared. Reaction

rates will also be much faster under hydrothermal conditions.

Fig. 5 shows, in a series of spectra, the effect of gradual acidification from pH 8.5 to pH 1.9 at room temperature. Both the $k^3\chi(k)$ (left half) and the corresponding Fourier transformations (radial structure plots, right half) are displayed. Acidification from pH 8.5 to a pH 8.1 slightly reduces the overall amplitude of the $\chi(k)$ function, as well as the intensity of the W–O peak at about 1.4 Å in the radial structure plot. There is an apparent decrease in the W–O distance. These trends continue upon further acidification to a pH 7.1. These trends are perhaps counter-intuitive because one would expect an increase in the amplitude of the $\chi(k)$ function and the intensity of the W–O peak when the number of next-nearest oxygen neighbors for the tungsten center increases from four to six upon formation of octahedrally coordinated isopolytungstates. As will be described in Section 3.2.2, this is due to destructive phase interference of multiple W–O distances. Furthermore, new interference patterns in the $\chi(k)$ function emerge at $k = 4$ Å^{-1} and $k = 10$ Å^{-1} at a pH of 7.1, and the radial structure plot shows an emerging additional peak near 3.2 Å. This additional peak arises from the proximity of neighboring W in

the new-formed isopolytungstates and from W–O multiple scattering contributions. Hence, these additional features become more pronounced at pH 5.5. The W–O peak in the radial structure plot, originally near 1.4 Å, has moved even further to a lower R-value. Preparation of a 0.2 molal sodium tungstate solution at pH 1.9 led to a solid precipitate (most likely $WO_3 \cdot 2H_2O$). The supernatant solution was decanted and an XAFS spectrum was obtained. The results are included in Fig. 5 and exhibit further drastic changes compared to the graphs for the pH 5.5 solution. There are additional XAFS oscillations at $k = 6$ Å^{-1} and $k = 8$ Å^{-1} and the oscillation near $k = 4$ Å^{-1} has significantly changed its shape. Interestingly, the W–O peak in the radial structure plot has moved back to a higher R-value although broadening might indicate several distinct distances. The W–W peak near 3.2 Å increased in intensity and there may also be an additional feature between $R = 2$ Å and $R = 3$ Å.

3.2.2. Model calculations

Purans et al. (1995) have analyzed XAFS spectra of several solid molybdenum and tungsten oxides and have identified single scattering paths from 1.7–
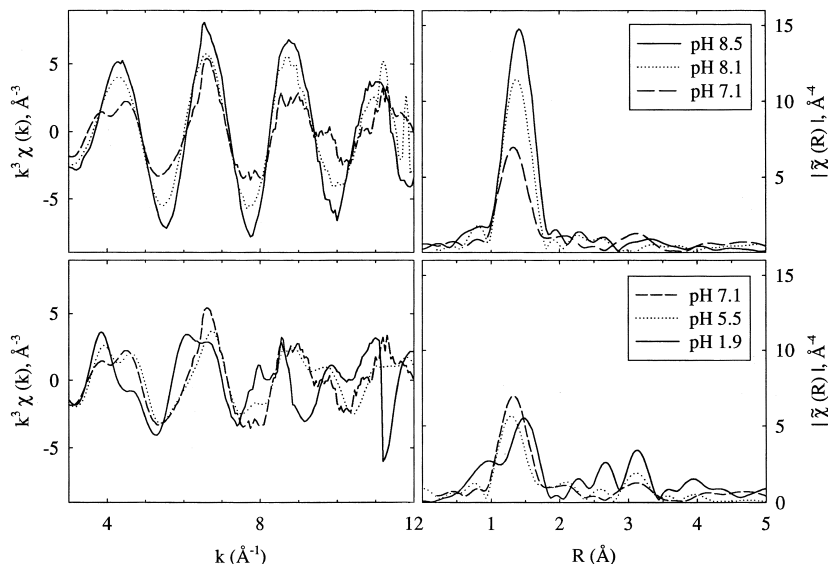

Fig. 5. The effect of acidification of a 0.2 molal Na_2WO_4 solution at room temperature for the $\chi(k)$ function on the left side and corresponding radial structure plot at the right side. The quite dramatic changes are described in detail in the text.

5.0 Å and a number of multiple-scattering paths as the main contributions. Hence, with increasing concentrations of isopolytungstates at lower solution pH, contributions from second-shell tungsten (W–W) and multiple scattering paths become increasingly important. In order to understand how these emerging contributions lead to the spectral changes described in Section 3.2.1, it is instructive to carry out a number of structural model calculations using the ab initio multiple scattering program FEFF (Zabinsky et al., 1995). For simplicity we chose for the simulations an approximate universal Debye–Waller factor of $\sigma^2 = 0.0015$.

First, we calculated the $\chi(k)$ function and corresponding radial structure plots for a W–O octahedron using the tungsten–oxygen bond distances 1.948 Å, 1.847 Å, 1.772 Å, 2.090 Å, 2.175 Å, 1.763 Å, found in the triclinic phase of WO_3 (Woodward et al., 1995), but fixing all bond angles at 90°. (There are angular distortions in the order of 10° present in the crystal structure of triclinic WO_3 reported by Woodward et al., 1995.) The average bond distance for this phase is 1.9325 Å. In the upper portion of

Fig. 6 we compare the contributions from single backscattering paths of this calculation (labeled solid WO_3) with the single backscattering paths of a W–O octahedron having six equal bonds at a distance of 1.9325 Å (labeled ''WO_6''), and a W–O tetrahedron with four equal bond distances of 1.8 Å (labeled WO_4^{2-}). While the W–O octahedron having the single bond distance of 1.9325 Å shows the expected larger amplitude in the $\chi(k)$ function and corresponding larger W–O peak in the radial structure plot, the W–O octahedron (WO_3) with several bond distances displays a much smaller amplitude and smaller W–O peak. Hence, for the spectra in Fig. 5, where we observed a decrease in $\chi(k)$ amplitude and W–O peak intensity upon acidification of the normal 0.2 molal tungstate solution, we can now attribute this observation to the large disorder in bond distances present in the isopolytungstates. Even though the two octahedrons (solid WO_3 and ''WO_6'') have the *same* average bond distance, they show in the upper portion of Fig. 6 large differences in phase shift. The phase shift of octahedral, multi-distance WO_3 is very close to that of the much shorter
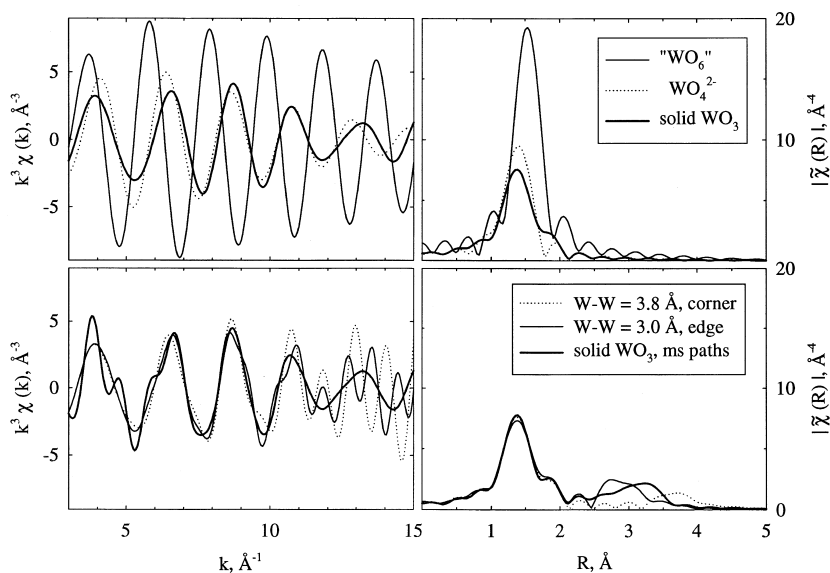

Fig. 6. Several calculated $\chi(k)$ functions (left half) and corresponding radial structure plots (right half). Upper portion: single scattering contributions from a W–O octahedron (''WO_6'') and W–O tetrahedron (WO_4^{2-}) with one bond distance of 1.9325 Å and 1.8 Å, respectively, and a W–O octahedron with six different W–O bond distances as found in solid WO_3. Lower portion: An additional tungsten atom was added to the WO_3 configuration: 3.8 Å away from the center along a corner (W–W = 3.8 Å, corner) and 3.0 Å along an edge (W–W = 3.0 Å, edge); and the effect of just adding multiple scattering paths to the WO_3 configuration is shown (solid WO_3, ms paths).

average-distance WO_4^{2-} spectra. Thus, the high degree of disorder, having a distinctly non-Gaussian distribution, has effects that are contrary to what one would expect from a treatment of this static disorder using a simple Debye–Waller type of disorder term. It is noteworthy, that the maximum of the W–O peak for WO_3 in the radial structure plot is at a *lower R*-value than for WO_4^{2-} even though the average W–O distance is significantly larger.

This result is not too surprising considering what is already known about the room temperature and pressure aqueous chemistry of tungstates. The formation of isopoly anions of a variety of metals (Nb^{5+}, Ta^{5+}, W^{6+}, Mo^{6+}, etc.) occurs through a process involving either or a combination of nucleophilic attack or nucleophilic attack followed by elimination of H_2O (Livage et al., 1988). For example, with tungstates, a protonated tetrahedrally coordinated tungstate group, HWO_4^-, undergoes nucleophilic attack by another HWO_4^- group producing one octahedrally coordinated W group and one tetrahedrally coordinated W group: $[(HO)O_3WO_2WO(OH)]^{2-}$ with an edge-shared linkage between the two groups. This ''polymerization'' process continues, forming compact cyclic oligomers containing edge-sharing octahedrally coordinated W groups, such as the paratungstate, pseudo-metatungstate, and metatungstate structures discussed above. For most cases, including that of isopolytungstates, the metal atoms in the octahedra are known to be displaced toward the outer (terminal) oxygen atoms (Cotton and Wilkinson, 1980) to minimize M–M interactions. This explains the non-Gaussian distribution in W–O bond distances for the structures that occur in our studies.

Second, we explored the effect of adding another tungsten atom near the W–O octahedron simulating contributions from adjoining octahedra in the polymer. For these simulations we chose the model octahedra having W–O distances equal to that of triclinic WO_3 because this provides the best qualitative agreement with the spectra in Fig. 5. In the lower portion of Fig. 6 we show the cases of corner-shared and edge-shared octahedra which we simulated by adding the extra tungsten atom at 3.8 Å and 3.0 Å along a corner and an edge octahedron, respectively. In both cases, the additional tungsten atom introduces a high frequency oscillation that becomes dominant at *k*-values greater than 11 Å^{-1}. For *k*-val-

ues below 11 Å^{-1}, the oxygen contribution remains dominant and the sinusoidal character of the $\chi(k)$ function remains preserved. (This does not change even in the most extreme and unrealistic scenario that the additional tungsten is placed along an edge at 2.5 Å^{-1} and the W–W Debye–Waller factor is set to 0.) The reason for the dominance of the oxygen backscattering contributions at low *k*-values is a different shape of the backscattering amplitude function $F(k)$ for oxygen and for tungsten (Teo, 1986; McKale et al., 1988). Hence, one can conclude that the multiple oscillations near 4 Å^{-1}, observed in Fig. 5 for pH < 7.1 solutions, cannot arise from tungsten–tungsten backscattering paths. Furthermore, one may be able to separately fit the W–W single scattering contributions at large *k*-values.

We were also not able to reproduce the multiple oscillations near 4 Å^{-1} by rearranging the six oxygen atoms to various different locations within the octahedron. However, inclusion of three linear multiple-scattering paths for the ''solid WO_3''-structure generated the $\chi(k)$ function also shown in the lower portion of Fig. 6. The addition of the linear multiple scattering paths (tungsten center–oxygen corner–opposite oxygen corner–tungsten center) causes interfering oscillations near 4 Å^{-1} and a broad peak above 3 Å in the corresponding radial structure plot. This observation demonstrates the importance of multiple scattering paths for interpreting the spectra of Fig. 5.

Overall, the sample calculations presented in this section show the sensitivity of XAFS to structural changes and, therefore, the ability to obtain in situ structural information. In the case of the complex species present in the chemical equilibria of isopolytungstates the sensitivity is particularly pronounced due to the large non-Gaussian distribution of bond distances that causes a large reduction in amplitude of the $\chi(k)$ function and the W–O peak in the radial structure plot.

3.3. Spectral changes with temperature of 0.2 molal sodium tungstate solutions at low pH

The 0.2 molal solutions of sodium tungstate at pH 5.5 and 1.9 were also heated to 200°C at a pressure of 235 bar. The experimental results shown in Fig. 7 are compared to the corresponding room temperature
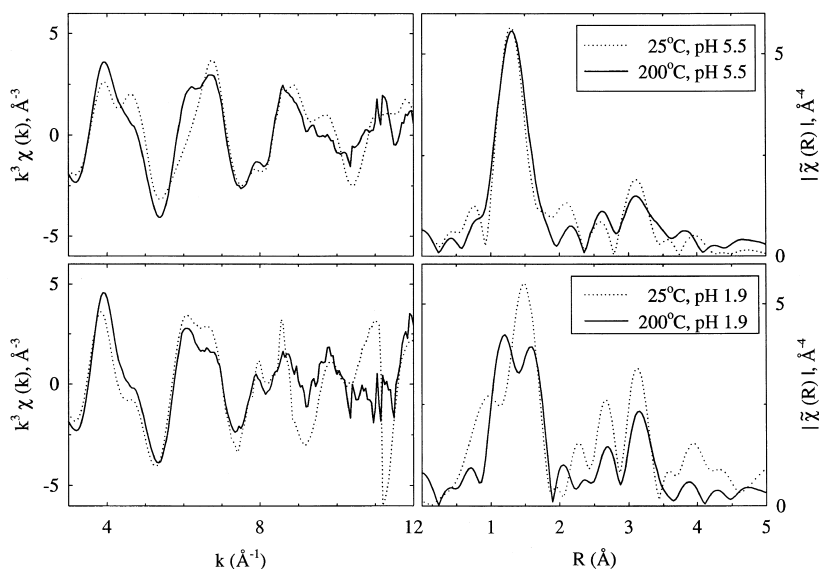
Fig. 7. The effect of increasing the temperature to 200°C (235 bar) on the $\chi(k)$ function (left side) of a 0.2 molal Na_2WO_4 solution of pH 5.5 (upper portion) and pH 1.9 (lower portion), and corresponding radial structure plots (right side). The pH values refer to the (starting) pH values measured at room temperature. The observations are described in detail in the text.

spectra. It was observed that the absorption edge heights of the pH 1.9 solutions gradually decreased ($\sim 10\%$) over time, which indicates a slow precipitation of a small amount of solid phase at 200°C. No changes in the XAFS $\chi(k)$ data were observed though. However, for the pH 5.5 solution the edge height and spectra were stable with time.

Temperature also has a significant effect on the observed $\chi(k)$ function and the corresponding radial structure plots. Particularly at low k-values, the $\chi(k)$ function of the pH 5.5 solution at 200°C becomes similar to the $\chi(k)$ function for the pH 1.9 solution (either 25°C or 200°C). However, the corresponding radial structure plot does not indicate an increase in the multiple scattering or W–W peak near 3.2 Å, at best, a slight decrease is observed instead. Considering the trends of the example calculations presented in the previous section, these observations may indicate a rearrangement of the isopolytungstate to a structural configuration more closely related to the structure of the isopolytungstates present at pH 1.9. For the pH 1.9 solution, there are only small changes in the $\chi(k)$ function with temperature although the corresponding radial structure plots indicate possible changes in the oxygen and tungsten coordination. It

is noteworthy that for both pH values neither the amplitude of the fine structure oscillations, nor the main W–O peak in the Fourier transform increases at 200°C. Therefore, the chemical equilibrium must still be dominated by polymer species at that temperature.

In summary, in situ XAFS studies of hydrothermal chemistry can provide important information on the structural changes that are occurring in these systems. It is important to realize however that the large amount of structural disorder present in the isopolytungstates makes a quantitative analysis of equilibrium constants a difficult (although maybe not impossible) task. Thus, for a full elucidation of this complex chemistry, it will be necessary to bring to bear complementary spectroscopic measurements on identical systems. The Raman study by Bilal et al. (1986) and the conductivity study by Wesolowski et al. (1984) suggest that the number of polymeric species present at elevated temperature is small, possibly only two, which would make this task not as complicated as it appears to be. It is unfortunate that these studies were carried out in the presence of mineralizers (NaCl) while our XAFS study is not. This will complicate a comparison of the data pre-

sented here with their findings. Further vibrational spectroscopic (Raman or IR) investigations would greatly aid in mapping out the polymerization chemistry. Also, the importance of knowing the in situ pH corresponding to each XAFS measurement cannot be overly emphasized. Calculating the in situ pH could be unreliable for systems of such complexity. Hence, in situ pH measurements would be preferable although these measurements are technically rather difficult. The scheme of using mono/dihydrogen phosphate as an internal pH standard as described by Bilal et al. (1986) may be a useful alternative approach to this problem. However, the presented XAFS data show that the tungsten monomer, one of the major equilibrium specie, remains tetrahedrally coordinated at elevated temperatures with an unchanged W–O bond distance. In addition, we have demonstrated that the presented data contain new structural information on the isopolytungstates present in aqueous solution at both low and high temperatures that will further our understanding of these systems.

3.4. Nickel bromide

Fig. 8 shows a series of X-ray absorption spectra, $\mu(E)$, for a 0.2 molal nickel(II)bromide solution introduced into the capillary cell (180 μm I.D., 340 μm O.D.) described in Section 2.4. The spectra represent single XAFS scans ($\sim$ 20 min) that were
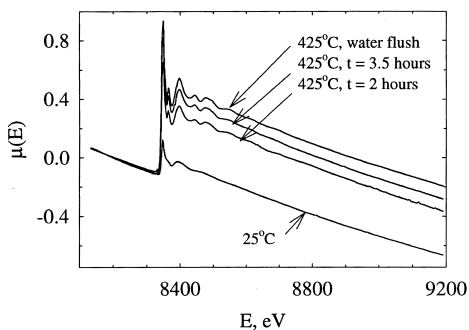

Fig. 8. Four single traces of X-ray absorption spectra, $\mu(E)$, at the nickel k-edge for a 0.2 molal NiBr$_2$ aqueous solution acquired in a fused silica capillary with 180 μm inner diameter. The data were acquired in the temporal sequence shown from bottom to top at 25°C, 425°C, 425°C at a later time, and 425°C after flushing of 5 ml of pure water. It is apparent that the nickel bromide solution reacted with the fused-silica capillary.
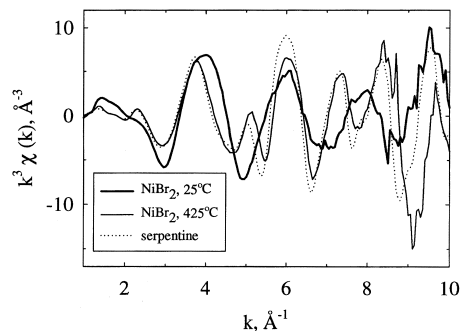

Fig. 9. The $\chi(k)$ function from the single-scan-spectra in Fig. 8 at 25°C and 425°C demonstrating the good quality of the spectra obtained in the fused-quartz capillaries. The included $\chi(k)$ function from a nickeliferous serpentine (Ni$_3$Si$_2$O$_5$(OH)$_4$) shows similarities to the 425°C spectrum, further supporting that a nickel silicate was formed.

taken in the sequence from bottom to top. The bottom spectrum was acquired at room temperature and it is identical to spectra of octahedrally coordinated Ni(H$_2$O)$_6^{2+}$ acquired in a conventional liquid cell (Wallen et al., 1998) previously reported. The sinusoidal pattern in Figs. 8 and 9 arises from six water molecules in the first hydration shell of the solvated Ni^{+2} ion. A constant small flow of 10 μl/min was maintained during heating of the capillary cell and acquisition of the spectra at high temperatures. The first spectrum acquired at 425°C spectrum looks dramatically different than that at room temperature, and it is also different from the 425°C aqueous solution spectrum reported by Wallen et al. (1998). The XAFS oscillations display a more complicated interference pattern that indicates the presence of several backscattering atoms at multiple distances. The edge height has dramatically increased from room temperature to 425°C. Several more spectra were subsequently acquired at 425°C, while still maintaining a flow of 10 μl/min. All of these spectra show the same XAFS pattern and a gradual increase in the edge height with time. We included the last of these spectra, acquired after 3 1/2 h, in Fig. 8. In the last step, the capillary was flushed with 5 ml of pure water at 425°C, completely removing any Ni^{2+} in the aqueous phase. As the top spectrum of Fig. 8 demonstrates, this did not remove the nickel from the capillary. On the contrary, the edge height increased further as about 2 ml more of

nickel bromide solution had to be flushed through the capillaries before being replaced by the pure water.

Figs. 8 and 9 demonstrate the high quality of the XAFS spectra taken in these capillaries. Some small glitches are discernable in particular for the spectra at 425°C. These may be mainly due to diffraction from the newly formed nickel silicate, which may have deposited non-uniformly onto the internal silica surface. The major glitch near 8380 eV may be a monochromator glitch. However, in all spectra, signal-to-noise is very reasonable for a single 20-min. scan. Therefore, in particular with the advent of third-generation synchrotron light sources, the small sample volume of the capillaries (tens of microliters) does not impose a limitation in sensitivity. Due to the small sample size (and/or concentration) the absorption is well below one absorption length and adverse amplitude distortions due to self-absorption effects is limited if not entirely absent. In turn, the stored energy in the small internal volumes of the capillaries is minute. Hence, handling of the capillary under pressure is safe with virtually no danger to the operator in the event of a cell failure.

The above-described observations indicate that the nickel bromide solution reacted irreversibly with the (dissolving) fused-silica capillary walls. The edge height of a XAFS spectrum is proportional to the number of absorbing atoms in the beam path. Approximately 2 h passed after the capillary heater was turned on and until the first scan was acquired. Each scan took about 20 min. Given the observation that the edge height increases continuously in time and approximately scales with the amount of nickel introduced into the cell by a steady flow, it appears that most if not all of the introduced nickel reacted with the fused-silica capillary.

Manning (1994) measured the solubility of quartz in water to very high temperatures and reported an expression for the equilibrium constant (K) of the reaction quartz = $SiO_{2(aq)}$. At 425°C log $mSiO_{2(aq)}$ is greater than -2, which represents a substantial amount of dissolved quartz in equilibrium with the solid quartz. Hence, most likely the reaction product is a nickel silicate. Manceau (1990) and Manceau and Calas (1986) studied nickel-bearing silicates with X-ray absorption spectroscopy. From this work, we included the k^3-weighted χ-function of a nickelifer-

ous serpentine ($Ni_3Si_2O_5(OH)_4$) in Fig. 9. While the serpentine data compares favorably to the spectrum at 425°C, XAFS data on $Ni(OH)_2$ (not shown, Manceau, 1990; Manceau and Calas, 1986) do not. Attempts are currently being made to definitively confirm the presence of a nickel silicate.

It is apparent that the above-described findings open up a number of potential applications for the use of fused-silica capillaries. The chemical interactions of nickel (or other metals) with silica at hydrothermal conditions as a function of temperature may be studied in situ using the fused-silica capillaries. The effects of further heating or cooling on the structure of the freshly generated nickel silicate could be investigated. Similar studies may be attempted with other cations or cation mixtures as well. For example, for applications to the vitrification of aqueous waste streams, silica or silicate-based powders, in addition to other components, are added to the aqueous phase prior to vitrification. It is generally assumed that reactions between the waste components and the silicate-based materials do not occur until the waste has been dried and the temperature elevated to the point where melting occurs. In view of the capillary results presented here, reactions between waste species and the silicate-based materials may occur at much lower temperatures under hydrothermal conditions, which may significantly influence the melting kinetics at much higher temperatures.

4. Summary and conclusions

Several new developments for XAFS as an analytical in situ tool for the study of hydrothermal systems have been presented. New experimental data to 400°C on 0.2 molal tungstate solutions were reported. These data were obtained in a new spectroscopic cell with a corrosion-resistant Pt/Ir insert. No changes with temperature were observed for tungstate solution with a starting pH of 8.5. Drastic changes were apparent in the XAFS data upon acidification, as this induces the formation of isopolytungstates. Raising the temperature of acidified solution also caused significant changes in the XAFS. FEFF-calculations were presented that demonstrate how

one can derive structural information on the species present in very complex isopolytungstate equilibria from the XAFS data at low and high temperatures. This approach may eventually lead also to a better quantitative assessment of the species present in the isopolytungstate equilibria.

It was also demonstrated how one could use inexpensive fused-silica capillaries to investigate hydrothermal systems. The fused-silica capillaries are safe and convenient to use and the inherent small sample volumes do not impose significant limitations in sensitivity. Specifically, it was observed in situ how a 0.2 molal nickel bromide solution irreversibly reacted with the fused-silica capillary to form a nickel silicate. Hence, the fused-silica capillaries may be used for a broad range of in situ studies of silicate formation under hydrothermal conditions.

Acknowledgements

References

Bai, S., Palmer, B.J., Yonker, C.R., Kinetics of deuterium exchange of resorcinol in D_2O at high pressures and high temperatures. Journal of Physical Chemistry A, in press.

Bassett, W.A., Wu, T.-C., 1998. Stability of hydration states and hysteresis of rehydration in montmorillonites as a function of temperature, H_2O pressure, and interlayer cations. Geophysical Monograph 101, 507–516.

Bilal, B.A., Haufe, P., Möller, P., 1986. Raman spectroscopic and electrochemical study of polymerization of tungsten (VI) in a hydrothermal solution up to 1 kbar and 200°C. Physica B 139–140, 721–724.

Brown, G.E., Calas, G., Waychunas, G.A., Petiau, J., 1988. X-ray absorption spectroscopy and its applications in mineralogy and geochemistry. In: Hawthorne, F.C. (Ed.), Reviews in Mineralogy. Spectroscopic Methods in Mineralogy and Geology 18 Mineralogical Society of America, Washington, DC, pp. 431–512.

Busey, R.H., Holmes, H.F., Mesmer, R.E., 1984. The enthalpy of dilution of aqueous sodium chloride to 673 K using a new heat-flow and liquid-flow microcalorimeter. Excess thermodynamic properties and their pressure coefficients. Journal of Chemical Thermodynamics 16, 343–372.

Collings, M., Sherman, D.M., Ragnarsdóttir, K.V., 1998. Complexation of Cu^{2+} in hydrothermal (25–175°C) NaCl brines: results from in situ EXAFS spectroscopy. Mineralogical Magazine 62A, 345–346.

Cotton, F.A., Wilkinson, G., 1980. In: Advanced Inorganic Chemistry. 4th edn. Wiley, New York, pp. 844–883.

Cyvin, S.J., 1968. In: Molecular Vibrations and Mean Square Amplitudes. Elsevier, Amsterdam, p. 71.

Darab, J.G., Smith, P.A., 1996. Chemistry of technitium and rhenium species during low-level radioactive waste vitrification. Chemistry of Materials 8 (5), 1004–1021.

Evans, H.T. Jr., 1971. Heteropoly and isopoly complexes of the transition elements of groups 5 and 6. In: Dunitz, J.D., Ibers, J.A. (Eds.), Perspectives in Structural Chemistry 4 Wiley, New York, pp. 35–59.

Fulton, J.L., Pfund, D.M., Ma, Y., 1996a. A diamond-window XAFS cell for studies of high-temperature, high-pressure aqueous solutions. Review of Scientific Instruments 67 (9), 1–5.

Fulton, J.L., Pfund, D.M., Wallen, S.L., Newville, M., Stern, E.A., Ma, Y., 1996b. Rubidium ion hydration in ambient and supercritical water. The Journal of Chemical Physics 105 (6), 2161–2166.

Greenwood, N.N., Earnshaw, A., 1984. Chemistry of the Elements. Pergamon, New York.

Huang, W.-L., Bassett, W.A., Wu, T.-C., 1994. Dehydration and hydration of montmorillonite at elevated temperatures and pressures monitored using synchrotron radiation. American Mineralogist 79, 683–691.

Kepert, D.L., 1973. Isopolyanions and heteropolyanions. In: Bailar, J.C. Jr., Emeléus, H.J., Nyholm, S.R., Trotman-Dickenson, A.F. (Eds.), Comprehensive Inorganic Chemistry. Pergamon, New York, pp. 641–656.

Kiddie, A.M., Wood, S.A., 1993. Raman spectroscopic studies of molybdate and tungstate solutions at elevated temperatures (25–300°C). In: Proceedings: 1991 symposium of chemistry in high-temperature aqueous solutions. pp. B2h1–B2h2, EPRI Report TR-102706.

Koningsberger, D.C., Prins, R., 1988. X-ray absorption: principles, applications, techniques of EXAFS, SEXAFS and XANES. Wiley, New York.

Livage, J., Henry, M., Sanchez, C., 1988. Sol–gel chemistry of

transition metal oxides. Progress in Solid State Chemistry 18, 239–341.

Manceau, A., 1990. Distribution of cations among the octahedra of phyllosilicates: insight from EXAFS. Canadian Mineralogist 28, 321–328.

Manceau, A., Calas, G., 1986. Nickel-bearing clay minerals: II. Intracrystalline distribution of nickel: an X-ray absorption study. Clay Minerals 21, 341–360.

Manning, C.E., 1994. The solubility of quartz in H_2O in the lower crust and upper mantle. Geochimica et Cosmochimica Acta 58 (22), 4831–4839.

McKale, A.G., Veal, B.W., Paulikas, A.P., Chan, S.-K., Knapp, G.S., 1988. Improved ab initio calculations of amplitude and phase functions for extended X-ray absorption fine structure spectroscopy. Journal of the American Chemical Society 110, 3763–3768.

Mosselmans, J.F.W., Schofield, P.F., Charnock, J.M., Garner, C.D., Pattrick, R.A.D., Vaughan, D.J., 1996. X-ray absorption studies of metal complexes in aqueous solution at elevated temperatures. Chemical Geology 127, 339–350.

Murata, T., Nakagawa, K., Kimura, A., Otoda, N., Shimoyama, I., 1995. Design of the cell and gas-handling system for the X-ray absorption study of supercritical fluid material. Review of Scientific Instruments 66 (2), 1437–1439.

Newville, M., Livins, P., Yacoby, Y., Rehr, J.J., Stern, E.A., 1993. Near-edge X-ray absorption fine structure. Physical Review B 48, 14126–14132.

Newville, M., Ravel, R., Haskel, D., Rehr, J.H., Stern, E.A., Yacoby, Y., 1995. Analysis of multiple-scattering XAFS data using theoretical standards. Physica B 208–209, 154–156.

Oelkers, E.H., Sherman, D.M., Ragnarsdóttir, K.V., Collins, C.R., 1998. An EXAFS spectroscopic study of aqueous antimony(III)-chloride complexation at temperatures from 25°C to 250°C. Chemical Geology 151 (1), 21–27.

Okada, K., Morikawa, H., Marumo, F., Iwai, S., 1974. Sodium tungstate. Acta Crystallographica B 30, 1872–1873.

Pfund, D.M., Darab, J.G., Fulton, J.L., Ma, Y., 1994. An XAFS study of strontium ions and krypton in supercritical water. Journal of Physical Chemistry 98, 13102–13107.

Purans, J., Kuzmin, A., Parent, Ph., Dexpert, H., 1995. XAFS analysis of the low symmetry octahedral molybdenum and tungsten oxides. Physica B 208–209, 307–308.

Ragnarsdóttir, K.V., Oelkers, E.H., Sherman, D.M., Collins, C.R., 1998. Aqueous speciation of yttrium at temperatures from 25°C to 340°C at P_{sat}: an in situ EXAFS study. Chemical Geology 151 (1), 29–39.

Seward, T.M., Henderson, C.M.B., Charnock, J.M., Dobson, B.R., 1995. The hydration of metal cations in hydrothermal solutions: recent EXAFS results. In: Kharaka, Chudaev (Eds.), Water–Rock Interaction. Balkema, Rotterdam, pp. 43–46.

Seward, T.M., Henderson, C.M.B., Charnock, J.M., Dobson, B.R., 1996. An X-ray absorption (EXAFS) spectroscopic study of aquated Ag^+ in hydrothermal solutions to 350°C. Geochimica et Cosmochimica Acta 60 (13), 2273–2282.

Sherman, W.F., Stadtmuller, A.A., 1987. Experimental techniques in high-pressure research. Wiley, New York.

Stern, E.A., Newville, M., Ravel, R., Yacoby, Y., Haskel, D., 1995. The UWXAFS analysis package: philosophy and details. Physica B 208–209, 117–120.

Suleimenov, O.M., Seward, T.M., 1999. Mn(II)chloride complexing up to 300°C using spectrophotometric methods. Chemical Geology, this issue.

Tamua, K., Inui, M., Hosokawa, S., 1995. XAFS measurements at high temperatures and pressures. Review of Scientific Instruments 66 (2), 1382–1384.

Teo, B.K., 1986. EXAFS, basic principles and data analysis. Springer, New York.

Wallen, S.L., Palmer, B.J., Pfund, D.M., Fulton, J.L., 1998. The ion pairing and hydration structure of Ni^{2+} in supercritical water at 425°C determined by X-ray absorption fine structure and molecular dynamics studies. Journal of Chemical Physics 108 (10), 4039–4046.

Wallen, S.L., Palmer, B.J., Pfund, D.M., Fulton, J.L., Newville, M., Ma, Y., Stern, E.A., 1997. Hydration of bromide ion in supercritical water: an X-ray absorption fine structure and molecular dynamics study. Journal of Physical Chemistry A 101 (50), 9632–9640.

Wallen, S.L., Pfund, D.M., Fulton, J.L., Yonker, C.R., 1996. High-pressure, capillary X-ray absorption fine structure cell for studies of liquid and supercritical fluid solutions. Review of Scientific Instruments 67 (8), 1–3.

Wesolowski, D., Drummond, S.E., Mesmer, R.E., Ohmoto, H., 1984. Hydrolysis equilibria of tungsten(VI) in aqueous sodium chloride solutions to 300°C. Inorganic Chemistry 23, 1120–1132.

Woodward, P.M., Sleight, A.W., Vogt, T., 1995. Structure refinement of triclinic tungsten trioxide. Journal of Physics and Chemistry of Solids 56 (10), 1305–1315.

Zabinsky, S.I., Rehr, J.J., Ankudinov, A., Albers, R.C., Eller, M.J., 1995. Multiple-scattering calculations of X-ray-absorption spectra. Physical Review B 52, 2995–3009.